ADVANCED MATERIALS TECHNOLOGIES
www.advmattechnol.de

Inclination-Enabled Generalized Microfluid Rectifiers via Anisotropic Slippery Hollow Tracks

Suwan Zhu, Xin Li, Yucheng Bian, Nianwei Dai, Jiale Yong, Yanlei Hu, Jiawen Li, Dong Wu,* and Jiaru Chu*

The power of spontaneous maneuvering of microfluids that allow gas or liquid to penetrate along a single direction, is usually endowed with the wettability gradient and the Laplace pressure difference through tailoring special solid–gas interfacial geographies. Herein, inspired by the structures on rice leaves and the slippery surfaces of the pitcher plant, anisotropic slippery hollow tracks (ASHTs) are fabricated and thus propose a class of unique inclination-enabled bubble "diode", on which one-way bubble penetration can be reversibly switched on/off. The minimum transition tilt angle is subject to the tract spacing and the infused oil amount. The underlying mechanism of bubble penetration is attributed to the competition between the variable buoyancy component and the interfacial energy gradient perpendicular to the samples. A wide spectrum of generalized microfluid maneuvering capabilities is further demonstrated, including heavy oil selective penetration, underwater CO_2 gas collection, and even dry/wet environment management in smart buildings, which are challenging for conventional counterparts. This framework should facilitate the development of microfluid control with favorable retainability and wide applicability in multiple fluids.

1. Introduction

The on-demand control of microfluids (droplets or bubbles) utilizing specific functional structures and materials[1,2] is fundamental to diverse scientific research and industrial processes, such as water–fog harvesting,[3] lab on a chip,[4] gas–liquid interfacial biochemical reaction,[5] oil–water separation,[6–9] permeable membrane/gating,[10,11] sustained drug release,[12] air purification,[13] froth management,[14] and others. Compared with droplet manipulation, bubble control has been proven to be challenging. This is usually because the gas is only approximately a thousandth the density of the liquid, so the spatial transport is susceptible to the surrounding viscous fluid environment. Therefore, powerful driving forces are preferred. Generally, the unidirectional and spontaneous transport of gas bubbles in planar surfaces can be achieved in two ways: one is the passive employment of the Laplace forces originating from the asymmetric structures (e.g., tapered or helical shapes) and wettability gradient.[15–19] The other is the active guidance of tunable external forces (e.g., magnetic, optical, or thermal fields) on the substrates and targeted gas bubbles.[20–24] Note that both strategies have their own advantages: the active control features fast bubble maneuvering and free motion direction, while the passive manner is pollution-free without the need for external energy and setups.

The degree of freedom for bubble maneuvering has been expanded since Lin et al. reported an interesting unidirectional water transfer effect using a special coating technique to create a wettability gradient across the fabric thickness.[25] Similarly, gas bubbles can also unidirectionally penetrate a membrane from one side to the opposite with asymmetric gas wettability along the thickness, which is termed bubble "diode" or bubble "Janus".[26–30] Due to the physical isolation of the membrane in the gas transport route, this platform is more suitable for phase-separation scenarios such as underwater gas collection.[15,29] However, almost all the present bubble diodes are limited to the creation of a wettability gradient on solid porous membranes, which is prone to collapse due to physical damage and the gradual absorption of the gas film on the aerophilic surfaces. Moreover, the introduction of a gas wettability gradient on solid walls is solely effective for the unidirectional penetration of gas bubbles rather than other fluids, such as heavy oil and water drops. These shortcomings significantly hinder their use in a wide variety of applications. Hence, there is an urgent need to develop generalized platforms that are capable of robust unidirectional transport for gas bubbles as well as diverse microfluids.

In this paper, we ingeniously connect the hierarchical solid structures of rice leaves with the slippery liquid-infused porous surfaces (SLIPSs) of the pitcher plant and thus propose unique

S. Zhu, Y. Bian, N. Dai, J. Yong, Y. Hu, J. Li, D. Wu, J. Chu
Key Laboratory of Precision Scientific Instrumentation of Anhui Higher Education Institutes
Department of Precision Machinery and Precision Instrumentation
University of Science and Technology of China
Hefei 230026, China
E-mail: dongwu@ustc.edu.cn
X. Li
State Key Laboratory of Pulsed Power Laser Technology
College of Electronic Engineering
National University of Defense Technology
Hefei 230000, China
E-mail: lixinkiller@nudt.edu.cn

The ORCID identification number(s) for the author(s) of this article can be found under https://doi.org/10.1002/admt.202300267

DOI: 10.1002/admt.202300267

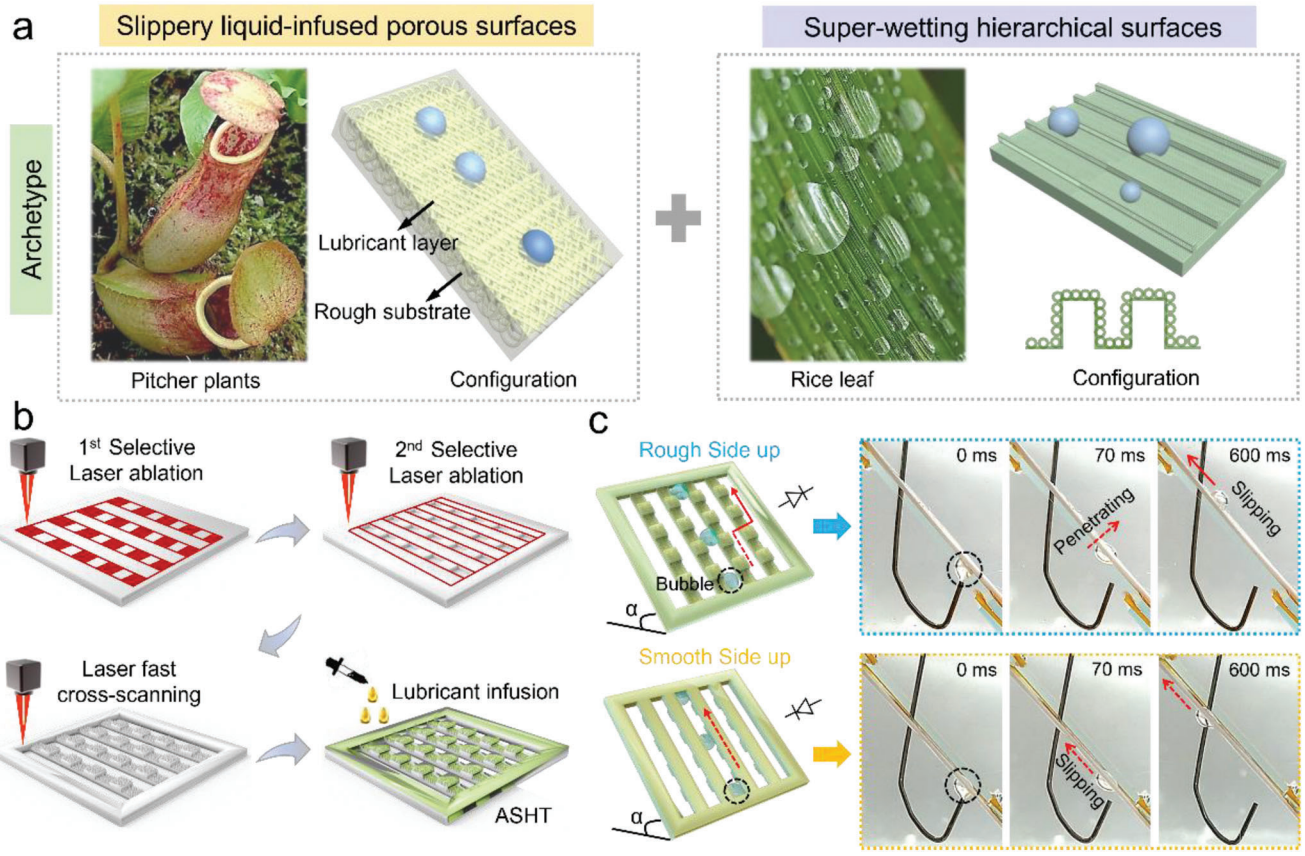

Figure 1. Conceptualized design of ASHTs. a) The interfacial design of ASHTs originates from two natural counterparts: the pitcher plant and the rice leaf. b) The ASHT fabrication process contains three-step femtosecond laser ablation and lubricant infusion. c) The ASHT exhibits the unidirectional penetration capability of underwater gas bubbles across the thickness.

inclination-enabled bubble diodes through anisotropic slippery hollow tracks (ASHTs) with robust liquid–gas interfaces. Relying on the self-repairing merit of SLIPSs and the underlying structural gradient, robust one-way bubble transport can be reversibly switched on/off via simply regulating the tilt angles. The minimum transition angle is subsequently revealed and is attributed to the competition between the variable buoyancy component and interfacial energy difference across the thickness. We further demonstrate the notable generalized microfluid rectification ability via this platform, including heavy oil one-way transport, underwater CO_2 gas collection, and even dry/wet environment management in smart buildings, which is otherwise impossible for conventional counterparts. This work should advance the current microfluidic control designs with favorable adjustability and generalized applicability.

2. Results and Discussion

2.1. Design and Characterization of ASHT Platform

In nature, the rough surface on *Nepenthes* pitcher plant with an aqueous lubricant layer endows itself with insect-capturing capability due to its excellent foreign matter repellency. On rice leaves, hierarchical nano-/microstructured grooves are found along the direction of the veins, leading to the anisotropic rolling phenomenon toward water droplets.[31,32] Inspired by the unique surface traits of these two natural species, we integrated the great-wall-like hierarchical rough structures with a slippery lubricant layer (**Figure 1**a,b), and thus proposed the ASHT microfluidic platform. Our ASHT is divided into two distinct parts: the solid anisotropic hollow tracks and a conformal slippery lubricant layer. To create solid anisotropic hollow tracks, a three-step femtosecond laser fabrication strategy was adopted (Figure 1b). The flat polytetrafluoroethylene (PTFE) sheets (thickness ≈500 µm) were first selectively ablated by femtosecond laser pulses to form discrete rectangular craters, followed by a second selective laser ablation to form hollow grooves. Afterward, the as-prepared samples were rapidly cross-scanned by laser pulses with an increase in the surface roughness. To form ASHT, the solid anisotropic hollow tracks were impregnated with a certain amount of silicone oil (viscosity ≈50 cSt) to preserve a similar frame.

The ASHT exhibits a notable unidirectional penetration capability of underwater gas bubbles across the thickness, as vividly depicted in Figure 1c. The underwater gas bubble would quickly penetrate the lower flat side to the upper side with the great-wall-like structures on the surface at a typical tilt angle of 45°. In the opposite orientation, the bubble would not penetrate the structured side and slip upward along the lower surface (Movie S1, Supporting Information). To verify the key factor that affects the selective transportation characteristic of ASHT, we carried out a

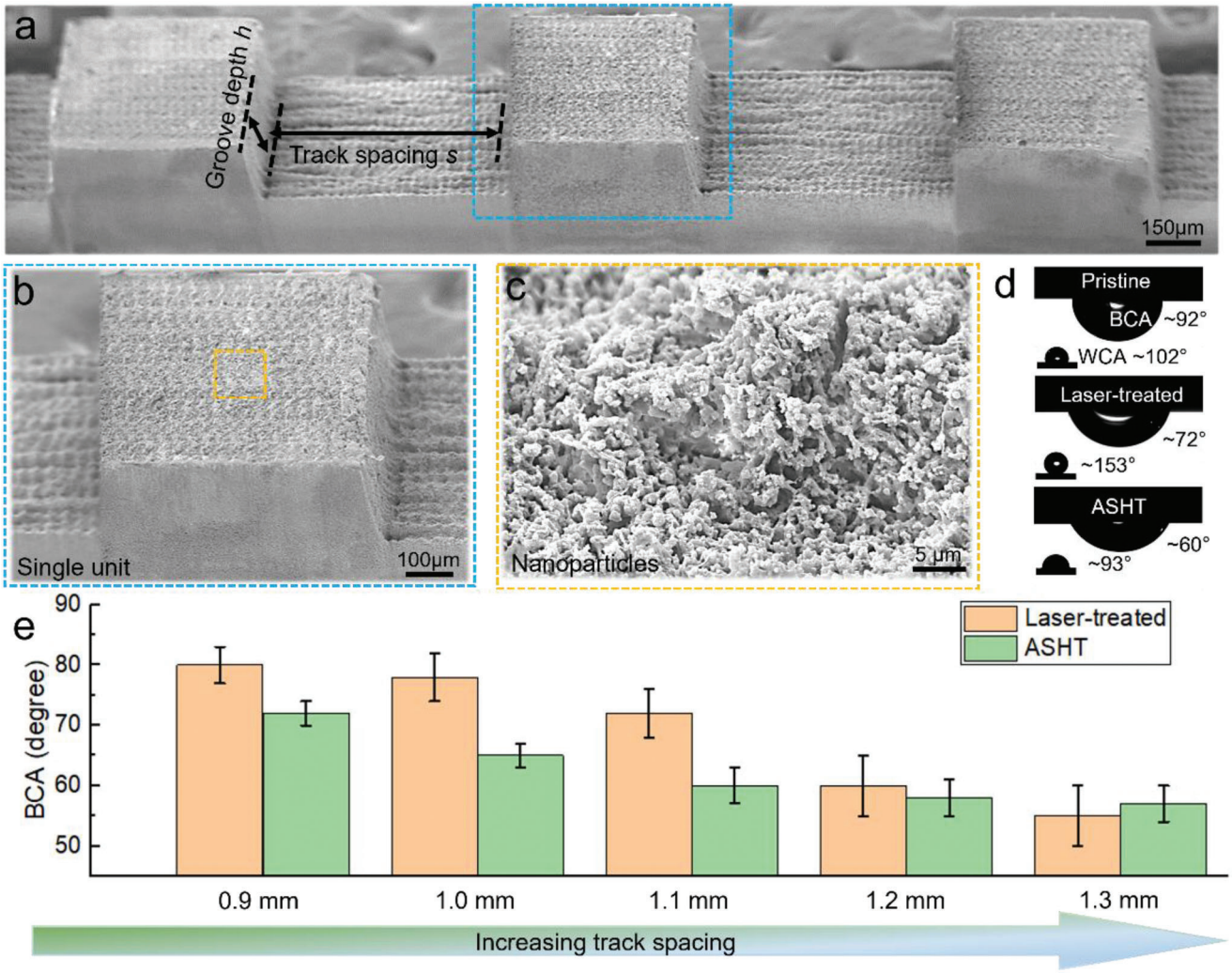

Figure 2. Characterization of morphology and BCAs on sample surfaces. a–c) High-resolution SEM images show various micropatterns and nanoparticles scattered on the surfaces of the great-wall-like frame. d) BCA decreased gradually from 92° to 60° at different ASHT fabrication stages. e) Disparity of BCAs on the solid skeletons and ASHTs with increasing track-spacing parameters.

contrast experiment by constructing a special ASHT, on which only the great-wall-like structures were replaced with flat rough structures after laser fast-scanning process on the smooth PTFE (Figure S1, Supporting Information). It was observed that the counterpart exhibited bubble impenetrability on both sides, indicating that the selective transport ability came from the unique great-wall-like structures on ASHT. It should be noted that the double-sided lubricant layers on ASHT are critical and are asymmetric on the two opposite sides, unlocking a class of new "gas diode" platforms without employing the surface energy gradient in most recently reported devices. A detailed discussion is provided further in later sections.

The morphology of the ASHT solid frame was investigated by scanning electron microscopy (SEM) at different magnifications, as shown in **Figure 2**a–c. The square-wave-shaped periodic microstructures formed by the insensitive femtosecond laser pulses, on which numerous edelweiss-like nanoparticles were observed. The formation of our multiscale structure, i.e., the combination of micro- and nanostructures, is prone to locking in place the infused lubricating fluid, which was already evidenced by the previous literature.[33] However, different from traditional SLIPSs that feature a uniform and flat lubricant layer, we created an uneven lubricant layer on the ASHT surface, forming a curved bubble-liquid interface and thus robust interfacial energy release on underwater gas bubbles. Bubble contact angles (BCAs) were measured on ASHT at different fabrication stages (Figure 2d). On pristine PTFE, BCA was measured as ≈92°. After laser selective ablation and lubricant infusion, BCA decreased from 72° to 60°. Figure 2e indicates the disparity of BCAs between laser-treated solid frames and ASHTs in varying track-spacing parameters. As the track spacing increased from 0.9 to 1.3 mm, the BCAs gradually declined on the laser-treated samples. For ASHTs, the values stabilized after dropping to ≈60°. Generally, the interfacial configuration, i.e., the contact angle for a liquid drop or a bubble on SLIPS, is rather complicated and can be influenced by many factors, such as the geography of the underlying microstructured solid wall and the lubricant layer.[34] In Figure 2e, as the track spacing increased, the solid substrate subsequently became

flatter, leading to a more uniform intercalating film. In this case, the solid structures do not directly affect the bubble geometry,[35] forming a stable BCA

2.2. Gas Maneuvering Characteristics on ASHTs with Diverse Parameters

We further examined the impact of diverse experimental parameters on the intriguing phenomena of the inclination-induced penetrating and slipping behaviors of gas bubbles on ASHT, including tilt angle, track spacing, and infusion oil amount (**Figure 3** and Movie S2, Supporting Information). Figure 3a shows that the working condition of the bubble diode, i.e., the selective unidirectional penetration of gas bubbles, is sensitive to the tilt angle and the infused oil amount, where a typical track spacing was set as 1.0 mm. Specifically, a smaller tilt angle (15°) would result in bubble vertical penetration on both sides of the ASHT. When the tilt angle increased to 30°, the gas bubble tended to pass through ASHT from the smooth side to the opposite side. For a constant tilt angle (60°), a less-lubricated sample would block the unidirectional passage of bubble movement.

Phase diagrams are elaborately quantified that concisely connect track spacing and oil amount with the unidirectional penetration behaviors of gas bubbles, as shown in Figure 3b. The lowermost boxes in different colors and shapes are defined as four different states of bubble motion: (1) detachment from the track when bubbles accumulate (red dotted), (2) start to slip when bubbles accumulate (blue dotted), (3) unidirectional penetration (light-green solid), and (4) nonoriented movement (light-purple solid). Apparently, only light-green solid regions represent an "on" state for a bubble diode. As mentioned earlier, a 15°-tilt-angle ASHT would not activate the bubble diode function. When the tilt angle increased to 30°, a narrow spectrum arose at track spacing = 1.0 mm, indicating an "on" state for bubble diodes. Moreover, the increase in track spacing would further enlarge the "on" state region for a bubble diode. At a critical angle of 75°, the bubble diode would work so long as the track spacing was greater than or equal to a characteristic value of ≈1.0 mm.

The interfacial dynamics of a slipping bubble on ASHT are sensitive to the infusion oil amount (bottom right in Figure 3b). Here, we chose a typical track spacing value of 1.0 mm and a tilt angle of 60° for ASHT. When the oil amount was less than 0.1 mg mm^{-2}, the gas bubble tended to slowly slip upward along the lower surface of an ASHT without penetrating the thickness, which could be attributed to the significant interfacial dissipation between the bubble and ASHT. Once the oil amount was greater than 0.1 mg mm^{-2}, the bubble–ASHT interfacial friction was prominently reduced, so the bubble diode started to work. A maximum capillary wicking of 0.5 mg mm^{-2} was observed on the current sample.

In the end of this section, we briefly discussed the effect of the width of the air channel and the patterned track on the bubble penetration behaviors. Here, five width ratios of air channel versus patterned track were employed as 0.8:1.6 mm, 1.1:1.3 mm, 1.4:1.0 mm, 1.7:0.7 mm, and 2.0:0.4 mm, respectively. According to the bottom right subgraph in Figure 3b, the typical track spacing and oil amount were set as 1.0 mm and 0.2 mg mm^{-2}, respectively, and the tilt angle was set as 60°. For the samples with width ratios of 0.8:1.6 mm and 1.1:1.3 mm, no bubble penetration was found on both sides across the thickness, which could be attributed to the fact that a narrow air channel would provide more resistance for bubble penetration on both sides. When the width of air channel increased to 1.4 mm, the sample started showing typical bubble "diode" characteristics. As the air channel width exceeded 1.7 mm, the sample exhibited double-sided bubble penetration, demonstrating the disappearance of the force barrier along the thickness (Figure S2, Supporting Information).

2.3. Unidirectional Gas Penetration Mechanism on ASHT

Unlike previous bubble diode/Janus designs that rely on the construction of a surface energy gradient and the Laplace pressure difference across the sample thickness, the preferential penetration behaviors of gas bubbles on ASHTs originate from the asymmetric gas–liquid contact areas on the two opposite sides, even though the per-unit interfacial energies are identical. On an ASHT, a gas bubble tends to penetrate the thickness from the smooth side onto the great-wall-like side. First, we experimentally visualized the instantaneous 2D-triple-phase contact lines/interfaces for gas bubbles on ASHTs (**Figure 4**a) as well as the 3D schematic diagram (Figure 4b). As clearly depicted in the figure, two different shapes of gas–liquid interfaces formed as the bubble initially contacted the two sides of ASHTs. On the smooth side, the gas–liquid interface is flat and consists of two identical and parallel segments. For the rough side, the contact areas are rather sophisticated and contain at least six segments, assuming that the bubble diameter is comparable to the periodic spacing of the microstructure array.

We next focused on the physical properties of the two distinct contact interfaces. Numerical simulations of the pressure distribution in an ambient water environment are given in Figure 4c. Due to the existence of the pressure and gravity gradient, the bottom of underwater bubbles tends to deform and escape. Here, the deformation-induced escaping behavior of the bubble is exclusively induced by the pressure difference distributed in bubble–water interfaces because the chemical wettability is identical on a SLIPS. Under the fluid gravity field, the pressure at the center of the bubble is the largest, and the pressure at the boundary gradually approaches that of the liquid environment. In the two separate structures in Figure 4c, the lower configuration changes more violently at the solid–liquid–gas interface (red arrow) than the upper configuration. As a result, the smooth-side-attached bubble is much easier to collapse/spread in the vicinity of the triple-phase interface, as indicated by the two bumps.

The bubble-driving force along the penetration direction can be essentially attributed to the minimization principle of interfacial energy.[36] During the spontaneous penetration of gas bubbles across the ASHT thickness, the area change of the gas-lubricant interface is decisive and is defined as $\Delta S = \Delta S_r - \Delta S_s$, where ΔS_r is the gas-lubricant contact area of a bubble-rough-side adhesion state, and ΔS_s is the gas-lubricant contact area of a bubble-smooth-side adhesion state. Thus, we obtained the interfacial energy release as:[37]

$$\Delta E = \gamma_{lg} \times \Delta S = \gamma_{lg} \times \left(\Delta S_r - \Delta S_s\right) \quad (1)$$

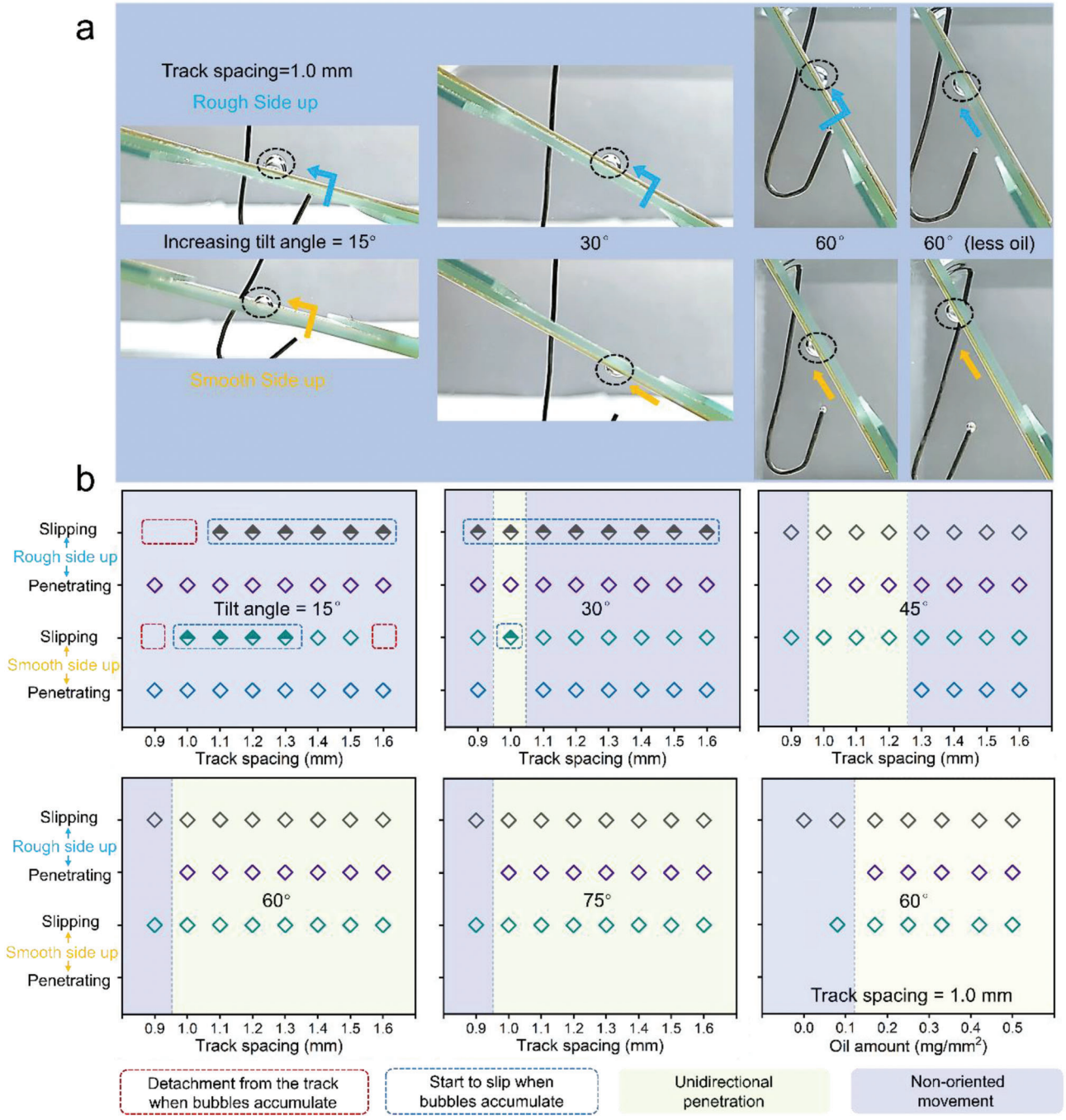

Figure 3. Inclination-induced penetrating and slipping behaviors of gas bubbles on ASHTs. a) The unidirectional penetration of bubbles is sensitive to the tilt angle and the infused oil amount, as evidenced by the photographic snapshots. b) Phase diagrams are elaborately quantified that concisely connect track spacing and oil amount with the penetrating and slipping behaviors. The semisolid and empty diamond symbols represent the bubble slipping and penetrating states corresponding to their left labels of y-coordinate, respectively. The specific bubble motion behaviors with colored boxes are indicated on the bottom.

where γ_{lg} represents the interfacial energy between the lubricant layer and the gas layer. Note that the exact contact area variation is not a constant and is related to various parameters, such as bubble volume, groove depth, and track spacing. Assume that a gas bubble is just stuck in the center of two adjacent track grooves (Figure 4a,b). Thus, the minimum ΔS should be 4 *sh*, where *s* is the track spacing and *h* is the groove depth. Based on these fixed physical quantities, the minimum energy release was calculated as $\approx 1 \times 10^{-8}$ J.

Returning to the inclination-sensitive one-way bubble penetration in both Figures 1 and 3, which can now be naturally interpreted by the competition (i.e., resultant force) between the

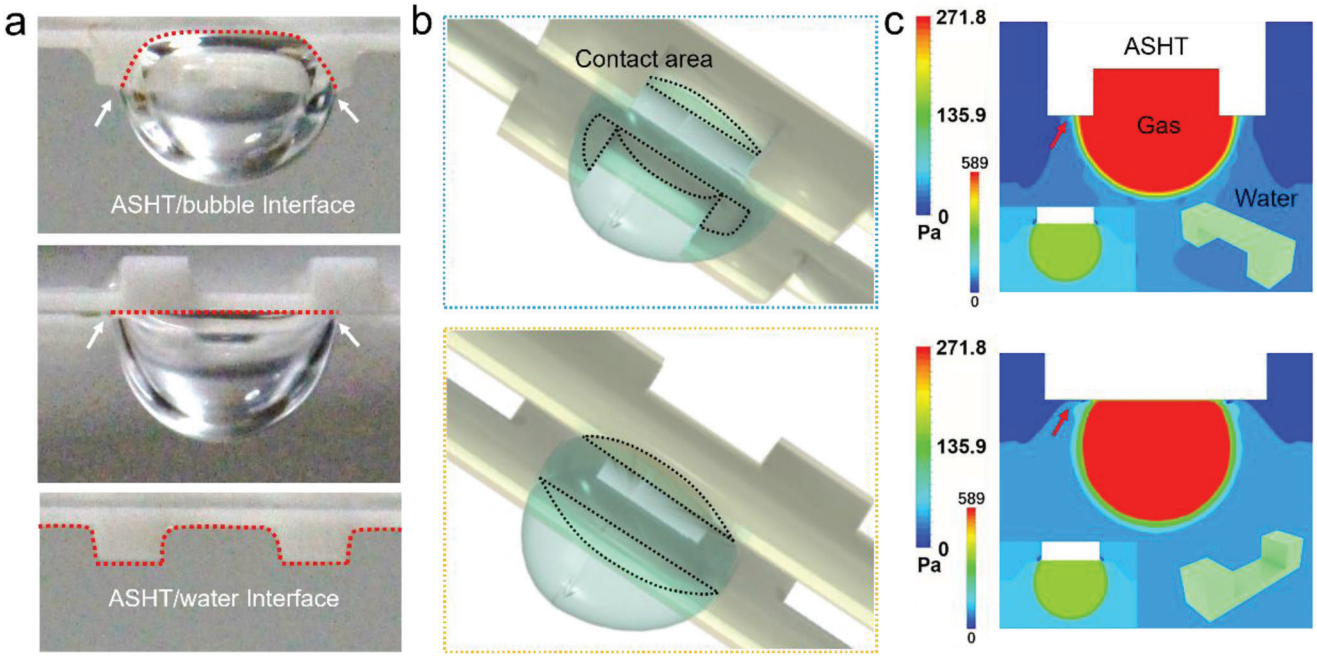

Figure 4. Triple-phase contact interfaces on bubble-attached ASHTs: a) photographic snapshots, b) schematic diagram, and c) numerical simulation of the pressure distribution in an ambient water environment.

variable buoyancy component and interfacial energy difference along the thickness. As the tilt angle increases from 0° initially, the buoyancy component perpendicular to the ASHT surface decreases. When the tilt angle reaches the maximum of 90°, the buoyancy component vanishes, and thus the bubble-driving force is solely determined by the interfacial energy difference across the thickness. Note that (1) the interfacial energy gradient force always exists on an ASHT-attached bubble, (2) the buoyancy is usually greater than the interfacial energy gradient force, and (3) the direction of the buoyancy component is opposite to that of the interfacial energy gradient force while the structured side faces down. Consequently, a structured-side-attached bubble will work in a "cutoff" state as long as the tilt angle reaches a threshold. The minimum transition angle is usually difficult to be quantified by the two-force competition due to the fact that the interfacial energy difference is very sensitive to diverse parameters, such as the geometries of the substrates, bubble profile/volume, and lubricant fluid characteristics.

2.4. Versatile Applications of Generalized Microfluid Rectifier

Relying on this powerful bubble management platform, a proof-of-concept model for generalized microfluid rectifier is further revealed, including heavy oil selective penetration, underwater gaseous carbon harvesting, and even dry/wet environment management in smart buildings, which are highly favored in current trends of carbon neutralization and energy-saving requirements. **Figure 5**a demonstrates the universality of selective penetration for heavy oils (ethylene dichloride: EDC, and chloroform) on ASHT at a tilt angle of 60°. Similar to the bubble diode function of ASHT, the heavy oil droplets could not penetrate ASHT from the microstructured side to the opposite side and slipped downward along the upper surface (Movie S3, Supporting Information).

Next, we integrated a tailored circular ASHT inside a transparent pipe and showed the function of an inclination-induced gas one-way valve (Figure 5b), which laid the foundation for underwater gaseous carbon (CO_2) collection (Movie S4, Supporting Information). Figure 5c vividly exhibits the process of gaseous carbon capture and chemical reaction between CO_2 gas and alkaline phenolphthalein solution utilizing our gas one-way valve. As sketched on the left, a pure CO_2 flow was generated from a compressed gas station and was then injected into the ASHT-integrated pipe connected to a beaker containing NaOH solution. The water-immersed ASHT was mounted inside an inverted acrylic cup bottom at a tilted angle of 45°. The exhaust gas flux was reduced through a relief valve at ≈300 μL min^{-1}. The evolution of carbon capture was readily visualized by the acid–base color reaction at 20 °C room temperature. The reaction between carbon dioxide and sodium hydroxide is described by:

$$CO_2 + 2NaOH = Na_2CO_3 + H_2O \quad (2)$$

As the acidic gas continuously flowed into the alkaline solution, the pH value gradually decreased, corresponding to the decolorization of phenolphthalein. Finally, the color of the alkaline phenolphthalein solution turned transparent after 30 min. In contrast, a smooth-side-up counterpart showed neither gas penetration nor color fading for the alkaline solution (Movie S5, Supporting Information).

Finally, we presented proof-of-concept ecological environment management in a smart building constructed using transparent acrylic boards. Two identical ASHTs with rough-side up were

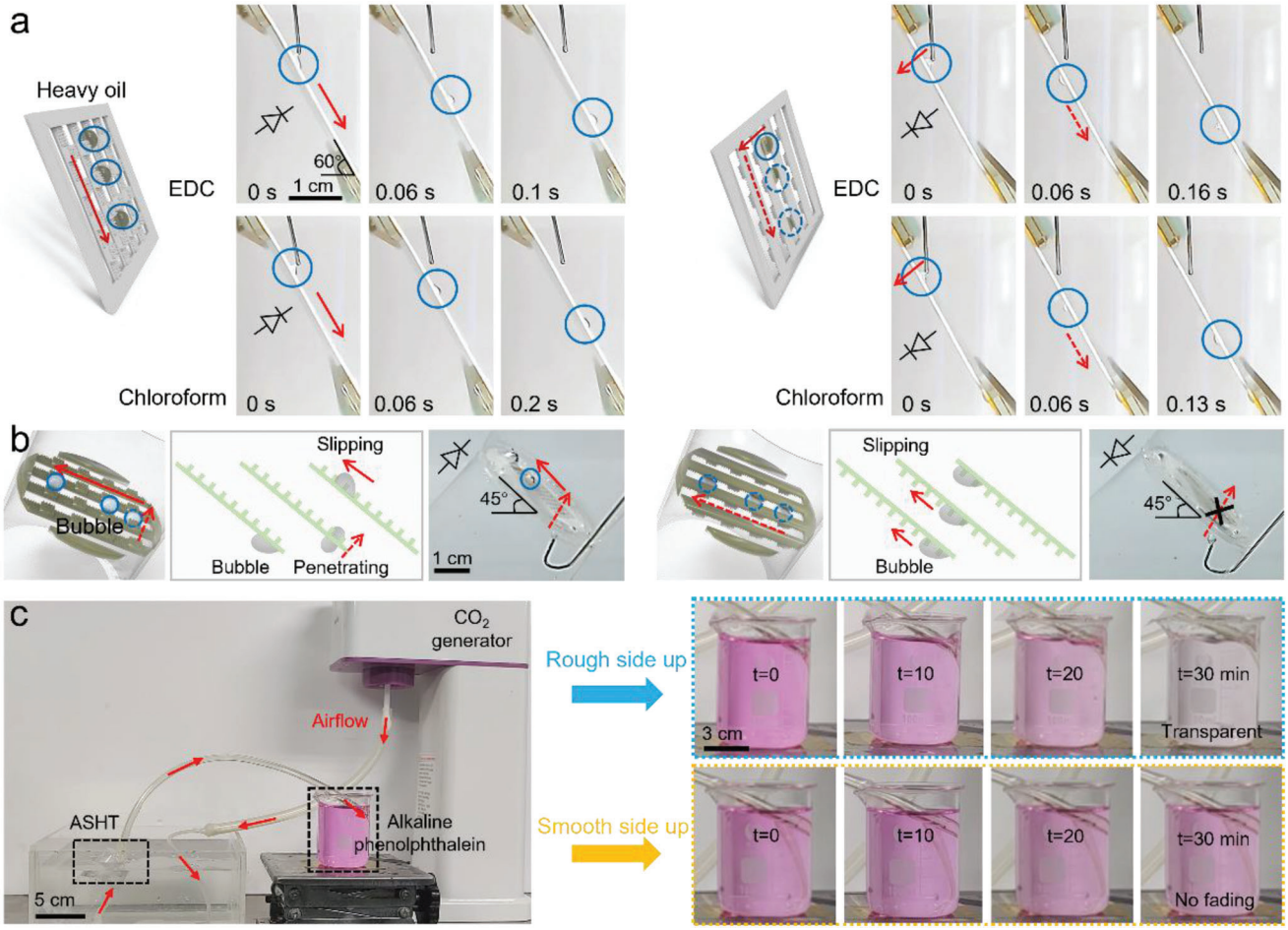

Figure 5. A wide spectrum of multiple fluids manipulation utilizing these versatile ASHT platforms, including: a) heavy oil selective penetration, b) gas selective passage, and c) underwater CO_2 gas collection and the following color reaction.

integrated on the colored roof tops with distinct tilt angles of 45° (reddish brown) and 15° (light blue), below which two separate areas (i.e., the working area and the green area) were set (**Figure 6**a). The track spacing and oil amount were set as 0.9 mm and 0.2 mg mm^{-2}, respectively. Two independent periodic water droplet flows were created by medical drips at a fixed flow rate of ten drops min^{-1} above the roof top to simulate natural rainfall. To minimize the influence of droplet impact energy, the drip tips were very close to the ASHT upper surfaces. In the foregoing experiments, a typical ASHT would exhibit an on–off state transition for fluid penetration at an appropriate tilt angle. As a gradual increase in the amount of penetrating water droplets in the green area, the seeds of mung bean sprouted after 4 days with numerous green branches (Figure 6b). According to our supplemental experiments (Figure S3, Supporting Information), a 15°-tilted ASHT on the roof exhibited a relatively broad-penetration range toward "raindrop" flow rate (>96 drops min^{-1}), which should be tolerant of the complex conditions of natural precipitation. For the asymmetric roof tops found in modern architectures, our ASHT-integrated design provides a universal solution for passive indoor dry/wet management, featuring the advantages of low cost, low destruction, and energy consumption.

3. Conclusion

In summary, we propose an inclination-enabled generalized microfluid rectifier using robust self-repairing liquid–gas interfaces, which are inspired by natural counterparts from solid rice leaves and slippery pitcher plants. Different from conventional reported bubble diodes, this platform exhibits switchable on/off bubble penetration merit during inclination. The minimum transition angle between the two states is further investigated under different parameters, including track spacing and infused oil amount. We attribute this intriguing inclination-induced penetration to the competition between the buoyancy component and interfacial energy gradient perpendicular to the membranes. Based on this generalized microfluid rectifier, a series of straightforward and versatile applications are demonstrated, including heavy oil one-way transport, underwater CO_2 gas collection, and even dry/wet environment management in smart buildings, which are challenging for traditional approaches. It is anticipated that our ASHTs can be exploited for new microfluid control devices featuring favorable interfacial retainability and on-demand microfluidic maneuvering.

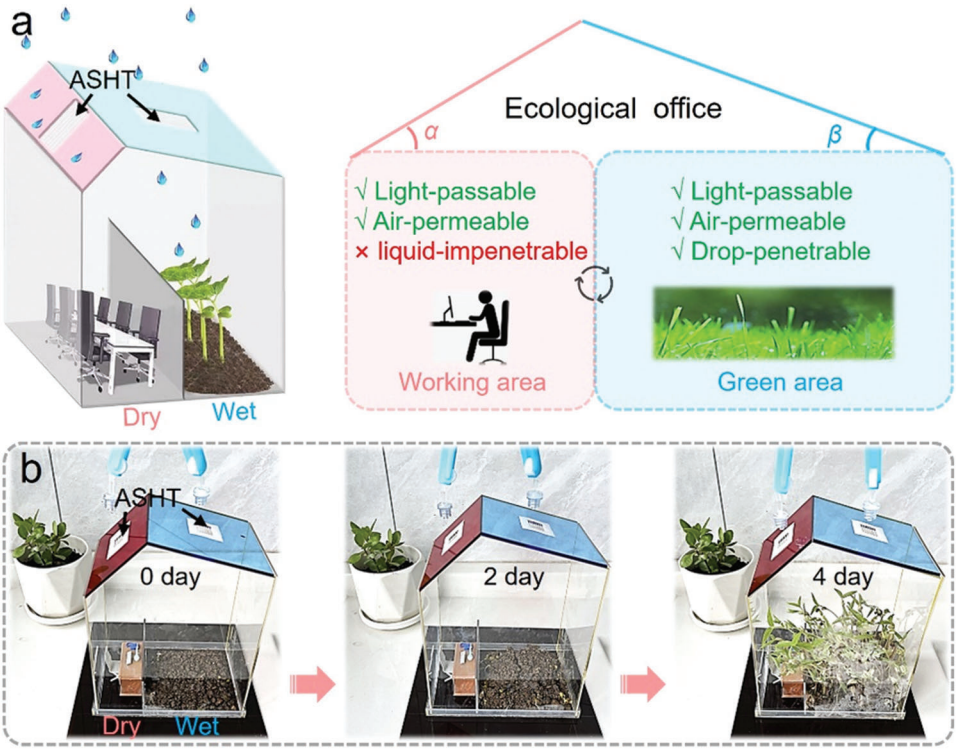

Figure 6. Unique demonstration of dry/wet environment management in smart buildings relying on ASHTs. a) Schematics show that dry and wet zones are independently maintained via two ASHTs on asymmetric roofs. b) The plant seeds eventually sprouted after a few days in the green area. Meanwhile, the adjacent working area remained dry.

4. Experimental Section

Materials: Polytetrafluoroethylene (PTFE) sheets (thickness ≈500 µm) were purchased from Bald Advanced Materials Tech. Co., Ltd., Hangzhou, China. The kinematic viscosity of silicone oil was 50 cSt at a temperature of 20 °C.

Femtosecond Laser Fabrication: A Ti:sapphire femtosecond laser system (Legend-Elite-1K-HE, Coherent, USA) was employed to fabricate the anisotropic hollow tracks following three steps: first selective laser ablation (forming the great-wall-like structures), second selective laser ablation (forming the hollow grooves), and third laser fast cross-scanning (increasing the surface roughness). The laser duration, repetition rate, and center wavelength were 104 fs, 1 kHz, and 800 nm, respectively. The laser scanning path was guided by a galvanometer scanner (ScanLab, Germany) equipped with a telecentric f–θ lens with a focal length of 63 mm. The laser cross-scanning power and speed were set as 300 mW and 5 mm s^{-1}, respectively.

Characterization: The surface morphology was characterized by a secondary scanning electron microscope (SEM, ZEISS EVO18). The bubble contact angle measurements were carried out by an optical contact angle meter (Innuo CA100C, China) in an ambient water environment at a typical volume of 4 µL. The average static contact angles were obtained by measuring five different positions on the same surface. The error bar took the arithmetic mean of the five measured values as the midpoint.

Numerical Simulation: To evaluate the mechanical properties of the fixed bubbles on different structures, the ambient pressure distribution was calculated through ANSYS software by adopting an implicit VOF multiphase flow model. The Boussinesq model was used for air density. We adopted the coupled algorithm to solve the whole Navier–Stoke equations. The flux difference splitting and multistep Runge Kutta schemes were adopted for spatial discretization and time discretization, respectively. The number of grid elements and nodes in the model was set as 1 000 000. The grid quality was greater than 0.99, and the iteration number was 400.

Supporting Information

Supporting Information is available from the Wiley Online Library or from the author.

Acknowledgements

This work was supported by the Open Research Fund of State Key Laboratory of Pulsed Power Laser Technology (grant No. SKL2021KF06), the Natural Science Foundation of Anhui Province (grant No. 2208085QE156), the National Natural Science Foundation of China (grant Nos. 61927814, 51805509, 52122511, 52175396, U20A20290), the National Key Research and Development Program of China (grant No. 2021YFF0502700), and the Major Scientific and Technological Projects in Anhui Province (grant No. 201903a05020005). The authors acknowledge the Experimental Center of Engineering and Material Sciences at USTC for the fabrication and measuring of samples. This work was partly carried out at the USTC Center for Micro and Nanoscale Research and Fabrication.

Conflict of Interest

The authors declare no conflict of interest.

Author Contributions

S.Z., X.L., and Y.B. performed the experiment. S.Z., X.L., N.D., and J.Y. analyzed the data. S.Z., Y.B., Y.H., J.L., and D.W. prepared and revised the

manuscript. D.W. and J.C. contributed the materials and experimental instruments.

Data Availability Statement

The data that support the findings of this study are available from the corresponding author upon reasonable request.

Keywords

bio-inspired surfaces, bubble manipulation, laser fabrication, microfluid rectifiers, unidirectional transport

Received: February 21, 2023
Revised: April 8, 2023
Published online: May 16, 2023

[1] Q. Zhang, X. Bai, Y. Li, X. Zhang, D. Tian, L. Jiang, *ACS Nano* **2022**, *16*, 16843.
[2] J. Zhang, B. Chen, X. Chen, X. Hou, *Adv. Mater.* **2021**, *33*, 2005664.
[3] C. Li, C. Yu, S. Zhou, Z. Dong, L. Jiang, *Proc. Natl. Acad. Sci. USA* **2020**, *117*, 23436.
[4] Y. Mao, Y. Pan, X. Li, B. Li, J. Chu, T. Pan, *Lab Chip* **2018**, *18*, 2720.
[5] X. Xiao, S. Li, X. Zhu, X. Xiao, C. Zhang, F. Jiang, C. Yu, L. Jiang, *Nano Lett.* **2021**, *21*, 2117.
[6] Z. Chu, Y. Feng, S. Seeger, *Angew. Chem., Int. Ed.* **2015**, *54*, 2328.
[7] Y. Wang, S. Yang, J. Zhang, Z. Chen, B. Zhu, J. Li, S. Liang, Y. Bai, J. Xu, D. Rao, L. Dong, C. Zhang, X. Yang, *Nat. Commun.* **2023**, *14*, 1108.
[8] X. Zhao, Y. Jiang, L. Cheng, Y. Lan, T. Wang, J. Pan, L. Liu, *Chinese Chem. Lett.* **2022**, *33*, 3859.
[9] M. Choi, S. Park, W. Choi, Y. Kim, K. Cho, J. Heo, M. Kim, H. Jung, Y. Jin, S. Lee, J. Hong, *NPJ Clean Water* **2022**, *5*, 48.
[10] W. Lai, L. Shan, J. Bai, L. Xiao, L. Liu, S. Wang, L. Gong, Y. Jiao, W. Xie, H. Liu, S. Luo, S. Zhang, *Chem. Eng. J.* **2022**, *450*, 137965.
[11] S. Yu, Y. Jing, Y. Fan, X. Hou, *Proc. Natl. Acad. Sci. USA* **2022**, *119*, e2206462119.
[12] J. Zhang, B. Liu, C. Chen, S. Jiang, Y. Zhang, B. Xu, A. Li, J. Xu, D. Wang, L. Zhang, Y. Hu, J. Li, D. Wu, J. Chu, Z. Shen, *ACS Appl. Mater. Interfaces* **2022**, *14*, 35366.
[13] Y. Zhang, Y. Han, X. Ji, D. Zang, L. Qiao, Z. Sheng, C. Wang, S. Wang, M. Wang, Y. Hou, X. Chen, X. Hou, *Nature* **2022**, *610*, 74.
[14] W. Wong, A. Naga, L. Hauer, P. Baumli, H. Bauer, K. Hegner, M. D'Acunzi, A. Kaltbeitzel, H. Butt, D. Vollmer, *Nat. Commun.* **2021**, *12*, 5358.
[15] S. W. Zhu, J. W. Li, S. W. Cai, Y. C. Bian, C. Chen, B. Xu, Y. H. Su, Y. L. Hu, D. Wu, J. R. Chu, *ACS Appl. Mater. Interfaces* **2020**, *12*, 18110.
[16] X. Tang, H. R. Xiong, T. T. Kong, Y. Tian, W. D. Li, L. Q. Wang, *ACS Appl. Mater. Interfaces* **2018**, *10*, 3029.
[17] X. Xiao, C. Zhang, H. Ma, Y. Zhang, G. Liu, M. Cao, C. Yu, L. Jiang, *ACS Nano* **2019**, *13*, 4083.
[18] C. H. Zhang, B. Zhang, H. Y. Ma, Z. Li, X. Xiao, Y. H. Zhang, X. Y. Cui, C. M. Yu, M. Y. Cao, L. Jiang, *ACS Nano* **2018**, *12*, 2048.
[19] C. Yu, M. Cao, Z. Dong, J. Wang, K. Li, L. Jiang, *Adv. Funct. Mater.* **2016**, *26*, 3236.
[20] S. W. Zhu, Y. C. Bian, T. Wu, C. Chen, Y. L. Jiao, Z. W. Jiang, Z. C. Huang, E. Q. Li, J. W. Li, J. R. Chu, Y. L. Hu, D. Wu, L. Jiang, *Nano Lett.* **2020**, *20*, 5513.
[21] C. Chen, Z. Huang, L. A. Shi, Y. Jiao, S. Zhu, J. Li, Y. Hu, J. Chu, D. Wu, L. Jiang, *Adv. Funct. Mater.* **2019**, *29*, 1904766.
[22] P. Guo, Z. Wang, L. Heng, Y. Zhang, X. Wang, L. Jiang, *Adv. Funct. Mater.* **2019**, *29*, 1808717.
[23] Y. Yan, Z. Guo, X. Zhang, L. He, Y. Li, K. Liu, J. Cai, D. Tian, L. Jiang, *Adv. Funct. Mater.* **2018**, *28*, 1800775.
[24] A. M. Rather, Y. Xu, Y. Chang, R. L. Dupont, A. Borbora, U. I. Kara, J. C. Fang, R. Mamtani, M. Zhang, Y. Yao, S. Adera, X. Bao, U. Manna, X. Wang, *Adv. Mater.* **2022**, *34*, 2110085.
[25] H. Wang, J. Ding, L. Dai, X. Wang, T. Lin, *J. Mater. Chem.* **2010**, *20*, 7938.
[26] C. Chen, L. A. Shi, Z. Huang, Y. Hu, S. Wu, J. Li, D. Wu, J. Chu, *Adv. Mater. Interfaces* **2019**, *6*, 1900297.
[27] S. Wu, D. Meng, C. Chen, L.-A. Shi, L. Zhou, Z. Huang, J. Li, Y. Hu, D. Wu, *Adv. Mater. Interfaces* **2019**, *6*, 1901176.
[28] C. T. Pei, Y. Peng, Y. Zhang, D. L. Tian, K. S. Liu, L. Jiang, *ACS Nano* **2018**, *12*, 5489.
[29] J. Yong, J. Zhuang, X. Bai, J. Huo, Q. Yang, X. Hou, F. Chen, *Nanoscale* **2021**, *13*, 10414.
[30] J. Huo, Q. Yang, J. Yong, P. Fan, Y. f. Lu, X. Hou, F. Chen, *Adv. Mater. Interfaces* **2020**, *7*, 1902128.
[31] T. S. Wong, S. H. Kang, S. K. Y. Tang, E. J. Smythe, B. D. Hatton, A. Grinthal, J. Aizenberg, *Nature* **2011**, *477*, 443.
[32] D. Wu, J.-N. Wang, S.-Z. Wu, Q.-D. Chen, S. Zhao, H. Zhang, H-B. Sun, L. Jiang, *Adv. Funct. Mater.* **2011**, *21*, 2927.
[33] J. S. Wexler, I. Jacobi, H. A. Stone, *Phys. Rev. Lett.* **2015**, *114*, 168301.
[34] S. Chapman, J. Hong, A. Waterhouse, C. Neto, *Chem. Soc. Rev.* **2020**, *49*, 3688.
[35] M. Kreder, D. Daniel, A. Tetreault, Z. Cao, B. Lemaire, J. Timonen, J. Aizenberg, *Phys. Rev. X* **2018**, *8*, 031053.
[36] P. Li, M. Cao, H. Bai, T. Zhao, Y. Ning, X. Wang, K. Liu, L. Jiang, *Adv. Funct. Mater.* **2019**, *29*, 1904446.
[37] B. E. Pinchasik, J. Steinkuhler, P. Wuytens, A. G. Skirtach, P. Fratzl, H. Mohwald, *Langmuir* **2015**, *31*, 13734.